Frozen fronts selection in flow against self-sustained chemical waves

T. Chevalier, D. Salin, and L. Talon
Laboratoire FAST, Université Paris–Sud, CNRS, Université Paris–Saclay, F-91405 Orsay, France
(Received 29 September 2016; published 24 April 2017)

Autocatalytic reaction fronts between two reacting species in the absence of fluid flow propagate as solitary waves. The coupling between an autocatalytic reaction front and a forced hydrodynamic flow may lead to a stationary front whose velocity and shape depend on the underlying flow field. We focus on the chemohydrodynamic opposition between forced advection and self-sustained chemical waves, which can lead to static stationary fronts, i.e., frozen fronts (FFs). Toward that end, we perform experiments, analytical computations, and numerical simulations with the autocatalytic iodate-arsenious acid reaction (IAA) over a wide range of flow velocities around a solid disk. For the same set of control parameters, we observe two types of frozen fronts: an upstream FF, which avoids the solid disk, and a downstream FF with two symmetric branches emerging from the solid disk surface. We map the range over which we observe these frozen fronts. We also address the relevance of the so-called eikonal, thin front limit to describe the observed fronts and select the frozen front shapes.

DOI: 10.1103/PhysRevFluids.2.043302

I. INTRODUCTION

Depending on the reaction kinetics, chemical reaction fronts display fascinating phenomena, such as Turing patterns, Belousov-Zhabotinsky oscillations, and chaotic or solitary wave propagation [1]. Autocatalytic reactions lead to fronts propagating as solitary waves with a constant velocity and invariant, flat, concentration profiles resulting from a balance between reaction and diffusion [1–3]. These fronts are analogous to flames in combustion [4], and autocatalytic reactions are a kind of "cold combustion model," especially in the thin flame limit. In contrast to flame propagation in combustion [4], where it has been analyzed thoroughly both theoretically and experimentally, the effect of fluid flow (laminar or turbulent) on reaction fronts has not been explored in detail until recently [5–20]. In the presence of a hydrodynamic flow, it has already been observed and understood that such fronts, while propagating at a new constant velocity, adapt their shape in order to achieve a balance between reaction diffusion and flow advection. More recently, the focus has been on the situation in which the flow field acted against the chemical reaction. In such a case, it has been observed over a wide range of flow velocity that the fronts are neither propagating forward (in the chemical reaction direction) nor blown in the flow direction, rather they remain static, frozen. In this dynamical equilibrium, chemistry and flow are both at work. For instance, in porous media [18–20], the front is pinned around the stagnation zones of the flow, due to the porous structure, and the front is curved in order to accommodate the local flow velocity fluctuations. In cellular flows, the frozen fronts are pinned in a vortex structure [13,21].

To visualize the frozen fronts (FFs), we designed an experiment using the iodate arsenous acid (IAA) chemical reaction in a simple heterogeneous forced flow field, namely a constant flow around a single disk-obstacle, opposed to the natural autocatalytic reaction front propagation. Depending on the control parameters, we observe two types of FF: one upstream FF, which avoid the solid disk, and one downstream FF with two symmetric branches emerging from the solid disk surface. We map the range over which we observe these frozen fronts. Numerical simulations provide a systematic phase diagram of the frozen fronts. Using the so-called eikonal limit of thin front thickness, we are able to account for the selection rule of the frozen fronts.

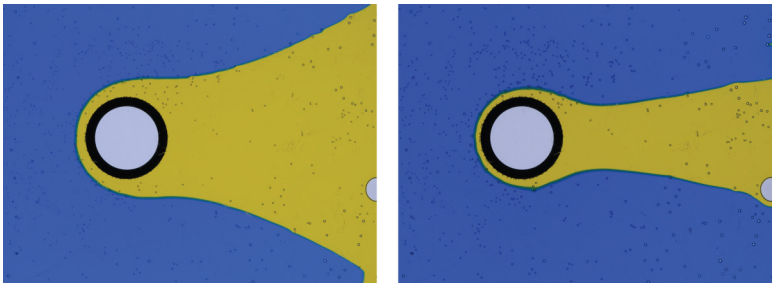

FIG. 1. Experimental frozen chemical front in a flow around a circular disk inside a Hele-Shaw cell. The fresh, blue reactant is injected from left to right at a flow at constant velocity U_0. The solid disk obstacle is a cylinder of diameter 17 mm. The burnt product is yellow. The front is made visible by the transition from blue to yellow. The chemical front in the absence of flow would propagate from right to left at a velocity V_χ. The two frozen fronts correspond to upstream fronts that avoid the solid for two different far field flow velocities: left: $U_0/V_\chi = -2.5$; right: FF for $U_0/V_\chi = -5$. The small dots in the images are bubbles.

II. EXPERIMENTS

We performed experiments using the iodate-arsenous acid (IAA) autocatalytic reaction:

$$3H_3AsO_3 + IO_3^- + 5I^- \longrightarrow 3H_3AsO_4 + 6I^-. \tag{1}$$

The reaction is autocatalytic in iodide (I^-). The concentrations used are $[IO_3^-]_0 = 7.5$ mM and $[H_3AsO_3]_0 = 25$ mM. As the ratio $[H_3AsO_3]_0/[IO_3^-]_0 > 3$, the arsenous acid is in excess [22] and the front can be localized by the transient iodine generated during the reaction. Instead of the usual method using starch to detect the transient iodine, we use polyvinyl alcohol (PVA) at a concentration of 6 kg/m^3, which is much more sensitive [23] and also provides good optical contrast (Figs. 4 and 9). In addition, we add to the fluids bromocresol green PH sensitive dye, which gives the location of the leading edge of the reaction front: its color is blue for reagents and yellow for products. In some experiments, we only use the latter front detection (Fig. 1).

This autocatalytic reaction in the fluid flow of local velocity $\vec{U}$ is governed by the convection (or advection) -reaction-diffusion equation, which can be written as

$$\frac{\partial C}{\partial t} + \vec{U}\,\vec{\nabla}\,C = D_m \triangle C + \frac{1}{\tau} f(C), \tag{2}$$

where the specific kinetics of the IAA reaction is third order [22]: $f(C) = C^2(1 - C)$. C is the concentration of the autocatalytic reactant (iodide), normalized by the initial concentration of iodate ($C = [I^-]/[IO_3^-]_0$), τ is the reaction time, and D_m is the molecular diffusion. In the absence of flow, $U = 0$ m/s, the balance between diffusion and reaction leads to a solitary wave of constant velocity V_χ and width l_χ [1,22,24], solutions of Eq. (2) given by

$$V_\chi = \sqrt{\frac{D_m}{2\tau}}, \quad l_\chi = D_m/V_\chi, \quad C = \left[1 + \exp -\left(\frac{x - V_\chi t}{l_\chi}\right)\right]^{-1}, \tag{3}$$

where x is the propagation direction of the wave. With the above concentration, we measure $V_\chi = (11 \pm 1)$ μm/s, from which we can infer the reaction front width, $l_\chi \simeq 200$ μm, using the molecular diffusion coefficient of water ($D_m = 2 \times 10^{-9}$ m^2/s). To achieve a quasi-two-dimensional velocity field, we use a Hele-Shaw cell [25], namely two thick rigid transparent parallel plates separated by a small gap (250 μm). The height of the solid circular disk of diameter $2R = 17$ mm is equal to the spacing of the joint squeezed between the two plates. A uniform flow field is achieved by injecting fluid into two inlets using two different pumps and letting it flow out of the cell through three outlets. In a Hele-Shaw cell, the velocity field (averaged over the thickness [26]) is, at leading order, the two-dimensional (2D) potential flow created by a uniform flow around a hydrodynamic

dipole [27], the intensity of which is linked to R. For a viscous fluid, the velocity is zero on solid boundaries, therefore there is a boundary layer of the order of the gap thickness: the variation of the velocity with the distance from the boundary can be approximated analytically [28]. We have also performed experiments in which the disk is replaced by a hydrodynamic dipole with an inlet and an outlet spaced by 5 mm where fluid is, respectively, injected and sucked at the same flow rate (see Fig. 4) and around. We have also performed experiments in which, instead of a disk, we use an air bubble (Fig. 9).

III. UPSTREAM FROZEN FRONT IN UNIFORM FLOW PAST A SOLID DISK

We have performed several series of experiments at different flow velocities U_0 in the direction opposite to that of the chemical wave without flow. Let us call $u = |U_0/V_\chi|$ the experimental control parameter. We first initiate the front at the left of the disk and let it propagate for a while; then, at a chosen time, we switch on the two pumps to generate a uniform flow. For $u < 1$, fronts propagate always toward the left and never stop, so that there is no FF. For $u > 1$, the front propagates toward the right and achieves a frozen front: Fig. 1 is a plot of such frozen fronts. The observed FF develops from "upstream" and avoids any contact with the disk surface. In Fig. 1 we see that the upstream front becomes closer to the solid as u increases. For $u \gtrsim 5-6$, the front cannot keep a stationary shape and hence no frozen fronts are observed: the forming front comes so close to the left of the solid disk that it comes into contact with it and then is transported by the flow to the right, hence limiting the range of accessible u values. For the u values leading to a frozen front, we have to account for the selection of its shape.

IV. FROZEN FRONT SELECTION USING THE EIKONAL EQUATION

In this section, we investigate the selection of the frozen front geometry, which can be explained from the eikonal equation including the finite curvature effect (i.e., $l_\chi \neq 0$). When the front width l_χ (200 μm in the experiment) is much smaller than the typical size of the system (here the disk radius $R = 8.5$ mm), the so-called eikonal equation accounts accurately for the front behavior [6,9]. It also corresponds to the thin flame regime in combustion. In this regime, Eq. (2) reduces [6] to the following expression of the normal component of the front velocity:

$$\vec{V}_F \cdot \vec{n} = \vec{U}(\vec{r}) \cdot \vec{n} + V_\chi + D_m\kappa = \vec{U}(\vec{r}) \cdot \vec{n} + V_\chi(1 + l_\chi\kappa), \tag{4}$$

where $\vec{U}$ is the local fluid velocity at the front position $\vec{r}$, $\vec{n}$ is the local unit vector normal to the interface (oriented from product to reactant), and κ is the curvature of the interface. The last term is particularly important in our study since it reduces the chemical velocity when the curvature is negative, as in Fig. 1. Frozen fronts satisfy

$$\vec{U}(\vec{r}) \cdot \vec{n} + V_\chi(1 + l_\chi\kappa) = 0. \tag{5}$$

Introducing the (x, y) Cartesian coordinate (x along the symmetry axis in the $\vec{U_0}$ direction) and the interface $h(y)$, it follows that

$$-\frac{v_x(h(y), y)}{\sqrt{h'(y)^2 + 1}} + \frac{h'(y)v_y(h(y), y)}{\sqrt{h'(y)^2 + 1}} + 1 - l_\chi \frac{h''(y)}{[h'(y)^2 + 1]^{3/2}} = 0, \tag{6}$$

where $\vec{v} = \vec{U}/V_\chi$ is the dimensionless velocity. The equation is thus an *implicit* second order differential equation that can be integrated once the initial conditions $h(0)$ and $h'(0)$ are known. Due to the symmetry of the problem, $h'(0) = 0$ so the frozen front is in principle a function of $h(0) = h_0$, which remains to be determined.

As l_χ is assumed to be small, one neglects generally the last term in the eikonal equation [16]. Such an assumption is only valid, from a mathematical point of view, if l_χ and D_m vanish at the same rate [see Eq. (3)], which is unlikely as the molecular diffusion is intrinsically a constant depending only on the involved fluids.

A. Eikonal equation without a curvature correction ($l_\chi = 0$)

The "classical" use of the eikonal equation [16] neglects the curvature term, which corresponds to setting $l_\chi = 0$ in Eqs. (5) or (6). The initial condition $h(0)$ must then satisfy the implicit equation

$$-v_x(h_0,0) + 1 = 0. \tag{7}$$

Once the initial condition h_0 has been determined, the complete interface can be deduced with a numerical forward method and by solving $h'(y)$ implicitly from

$$-v_x(h(y),y) + h'(y)v_y(h(y),y) + \sqrt{h'(y)^2 + 1} = 0. \tag{8}$$

It is important to remark at this point that the obtained solutions may have a nonzero curvature at $y = 0$. Our objective is now to determine the influence of l_χ and thus the curvature in the eikonal equation on the interface selection.

B. Eikonal equation with a curvature correction ($l_\chi \neq 0$)

We note that including the curvature term leads to degenerate solutions of Eq. (7). Indeed, the initial condition now reads $-v_x(h(0),0) + 1 - l_\chi h''(0) = 0$. The initial front position h_0, and thus the complete solution, hinges now on the initial curvature $h''(0)$, which is unknown and could *a priori* be considered as a free parameter. To determine the selection of $h(0)$, we make a Taylor expansion of the static eikonal equation in the vicinity of the apex of the frozen front ($y \simeq 0$) for the variables involved in Eq. (6), namely

$$h(y) = h(0) + \tfrac{1}{2}y^2h''(0) + \tfrac{1}{24}y^4h^{(4)}(0) + O(y^6), \tag{9}$$

$$v_x(h(y),y) = v_x(h(0),0) + \tfrac{1}{2}y^2[h''(0)\partial_x v_x(h(0),0) + \partial_{xx}v_x(h(0),0)] + O(y^4), \tag{10}$$

$$v_y(h(y),y) = -y\partial_x v_x(h(0),0) - \tfrac{1}{6}y^3[3h''(0)\partial_{xx}v_x(h(0),0) + \partial_{xyy}v_x(h(0),0)] + O(y^4), \tag{11}$$

where we have taken into account the x-axis symmetries, namely $h(y) = h(-y)$, $v_x(h(y),y) = v_x(h(-y),-y)$, and $v_y(h(y),y) = -v_y(h(-y),-y)$ and of the fluid incompressibility ($\partial_x v_x + \partial_y v_y = 0$). Equation (6) leads then to the polynomial expression

$$\begin{aligned}0 = {} & -v_x(h_0,0) + 1 - l_\chi h_0'' + y^2\left\{v_x(h_0,0)h_0''^2 - 3\partial_x v_x(h_0,0)h_0'' - \partial_{yy}v_x(h_0,0) + l_\chi\left(3h_0''^3 - h_0^{(4)}\right)\right\} \\ & + \frac{y^4}{24}\left\{6h_0''^2\partial_{yy}v_x(h_0,0) - 15h_0''^2\partial_{xx}v_x(h_0,0) - 10h_0''\partial_{xyy}v_x(h_0,0) + \left(18h_0''^3 - 5h_0^{(4)}\right)\partial_x v_x(h_0,0)\right. \\ & \left. + \left(4h_0^{(4)}h_0'' - 9h_0''^4\right)v_x(h(0),0) - \partial_{yyyy}v_x(h_0,0) - l_\chi\left(h_0^{(6)} - 30h_0^{(4)}h_0''^2 + 45h_0''^5\right)\right\} + O(y^6),\end{aligned}$$

where for compactness we use $h_0 = h(0)$, $h_0'' = h''(0)$, etc.

Since the terms at all orders should be equal to zero, it thus amounts to solving an infinite set of equations with an infinite number of unknowns, $\{h_0^{(2n)}, n = 0,1,\dots\}$. Interestingly, one can note that each order $0(y^{2n})$ involves the same order derivative, $h_0^{(2n)}$, but also the next one, $h_0^{(2n+2)}$. For instance, the leading order (y^0) involves $h(0)$ and $h''(0)$ and the second order (y^2) involves $h(0)$, $h''(0)$, and $h^{(4)}(0)$:

$$-v_x(h_0,0) + 1 - l_\chi h_0'' = 0, \tag{12}$$

$$v_x(h_0,0)h_0''^2 - 3\partial_x v_x(h_0,0)h_0'' - \partial_{yy}v_x(h_0,0) + l_\chi\left(3h_0''^3 - h_0^{(4)}\right) = 0. \tag{13}$$

Therefore, a method to construct an approximation consists in truncating the Taylor expansion at a given order n, and thus discarding the last term of order $(n+1)$. For instance, the zeroth-order truncation simply leads to solving the eikonal equation without the curvature correction Eq. (7). The

parabolic, second order truncation leads to the following system of equations:

$$-v_x(h_0,0) + 1 - l_\chi h_0'' = 0, \tag{14}$$

$$v_x(h_0,0)h_0''^2 - 3\partial_x v_x(h_0,0)h_0'' - \partial_{yy} v_x(h_0,0) + l_\chi\left(3h_0''^3\right) = 0, \tag{15}$$

and so forth.

It is also important to note that each equation depends strongly on the derivatives of the flow field. We expect thus that the choice of the order of truncation depends significantly on the spatial structure of the flow.

C. Numerical validation

To validate this analytical procedure, we integrate numerically the full eikonal equation, Eq. (4). The velocity field corresponding to a uniform flow around a 2D solid disk of radius R immersed in a uniform flow has simple analytical expressions (and thus explicit derivatives) [26,27]. In polar coordinates,

$$v_r(r,\theta) = \left(1 - \frac{R^2}{r^2}\right)U_0\cos\theta, \quad v_\theta(r,\theta) = -\left(1 + \frac{R^2}{r^2}\right)U_0\sin\theta, \tag{16}$$

where U_0 is the uniform far-field flow velocity, thus $u = U_0/V_\chi$. The front is initially flat and located far upstream from the disk. The integration is performed with the step forward direct method. As can be seen in the top left of Fig. 2, where the different fronts correspond to different evolution times, the front achieves an asymptotic frozen front geometry. The top right part of the same figure displays a series of FFs corresponding to different l_χ: the front geometry is observed to depend significantly on the chemical length l_χ. The larger l_χ is, the smaller is the distance (apex) of the front, $|h(0)|$, from the disk, in agreement with experiments (Fig. 1).

We compare now the achieved frozen front geometries to those obtained by our truncating procedure. In the bottom of Fig. 2, the measured values of the normalized apex coordinate at the axis, $|h_0|$ (square), and the corresponding curvature, h_0'' (diamonds), on the asymptotic frozen fronts are plotted versus l_χ/R. The solid curves correspond, respectively, to the zero, second, and fourth order truncation approximations. This clearly shows that increasing the truncation order asymptomatically converges toward the numerical results. Hence, for a given set of parameters $(u,l_\chi/R)$, the asymptotic FF, obtained from the dynamics of Eq. (4), can be characterized by the values $h(0)$ and the curvature $h''(0)$. We thus observe an excellent agreement between the truncation expansion and the numerical calculation for the selection of the frozen fronts. Moreover, Fig. 2 clearly shows that as $l_\chi \to 0$, both $h(0)$ and $h''(0)$ asymptotically converge to finite values, which correspond to the limit of the eikonal ones. To conclude, this procedure allows us to improve the "classical" use of the eikonal equation [16], which neglects the last term in Eq. (4): indeed, setting $l_\chi = 0$ in Eq. (4) does not mean that there is no front curvature but that the zero order approximation, $-v_x(h_0,0) + 1 = 0$, gives only the front position, $h_{l_\chi=0}(0)$.

In the same papers [16], a clever construction of the allowed fronts is described. In the full eikonal limit ($l_\chi = 0$), the front is initiated at the boundary of slow zones and is not allowed to penetrate them. These slow zones correspond to $|\vec{U}(\vec{r})| \leqslant V_\chi$. In Fig. 3, we have drawn the slow zone around the solid disk (red), and the eikonal frozen front ($l_\chi = 0$) corresponds to the blue solid line, which obviously follows the prescription.

V. COMPARISON WITH EXPERIMENTS USING A SOURCE-SINK CONFIGURATION

We want to test these predictions against the experiments. Due to the contact with the solid disk mentioned above, the range of accessible u values was limited. Therefore, we designed an analogous experiment that allows us to cover a wider range of u values. Remembering that the potential flow around a solid disk in a Hele-Shaw cell [see Eq. (6)] is the same as the one around a

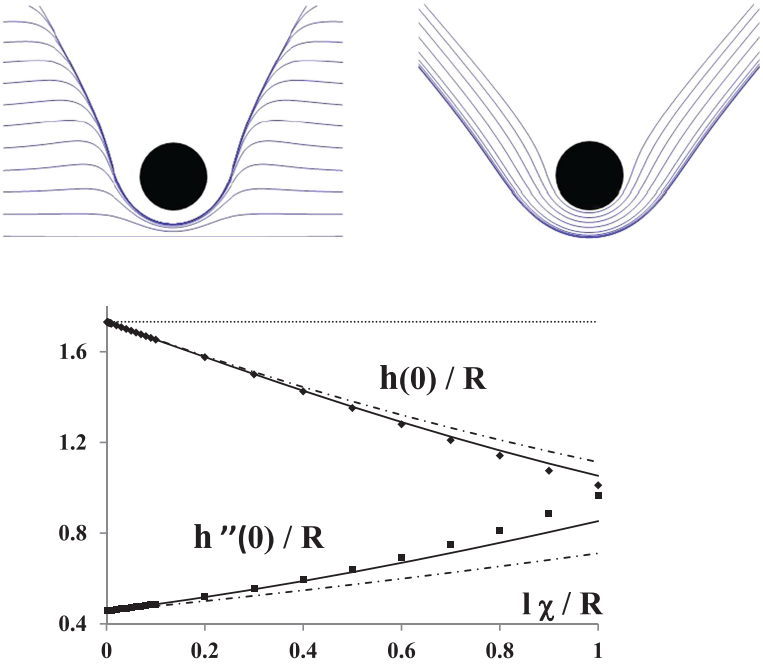

FIG. 2. Frozen chemical front for a flow around a disk determined by using the eikonal equation (4). Top left, views of the frozen front formation at different time steps from flat initial front ($t = 0$) to frozen front at long times ($t = \infty$) for $u = 2$ and $l_\chi/R = 0.1$. Top right: achieved static frozen front for $u = 1.5$ and for different values of l_χ/R increasing from 0 to 1; the larger the ratio, the closer the solid disk. Bottom: variations of the normalized distance $|h(0)|/R$ from the disk of the apex of the front (on the symmetry axis) and of its curvature versus l_χ/R: The squares and diamonds correspond, respectively, to $|h(0)|$ and $h''(0)$ measured on the achieved static FF. The dotted, dashed-dotted, and solid lines correspond, respectively, to the zero, second, and fourth order truncation approximations (see text) for the apex (top) and curvature (bottom).

hydrodynamic dipole (immaterial solid) [26–28], we designed such an experiment. The fresh, blue reactant is injected from left to right, as shown in Fig. 1, at a constant flow rate Q_0 and hence a constant flow velocity $U_0 = Q_0/(w\,e)$, where $w = 65$ mm and $e = 0.25$ mm, are, respectively, the

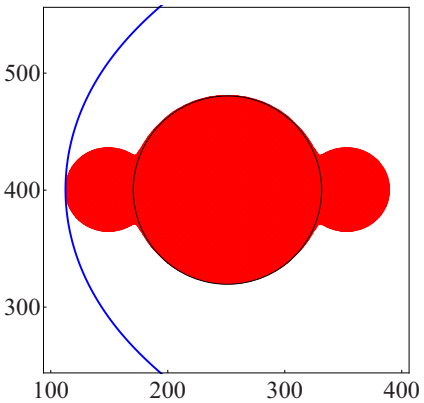

FIG. 3. The red zone around the solid disk (black circle) corresponds to the so-called slow zone [16], where $|\vec{U}(\vec{r})| \leqslant V_\chi$. The solid blue line corresponds to the eikonal frozen front ($l_\chi = 0$).

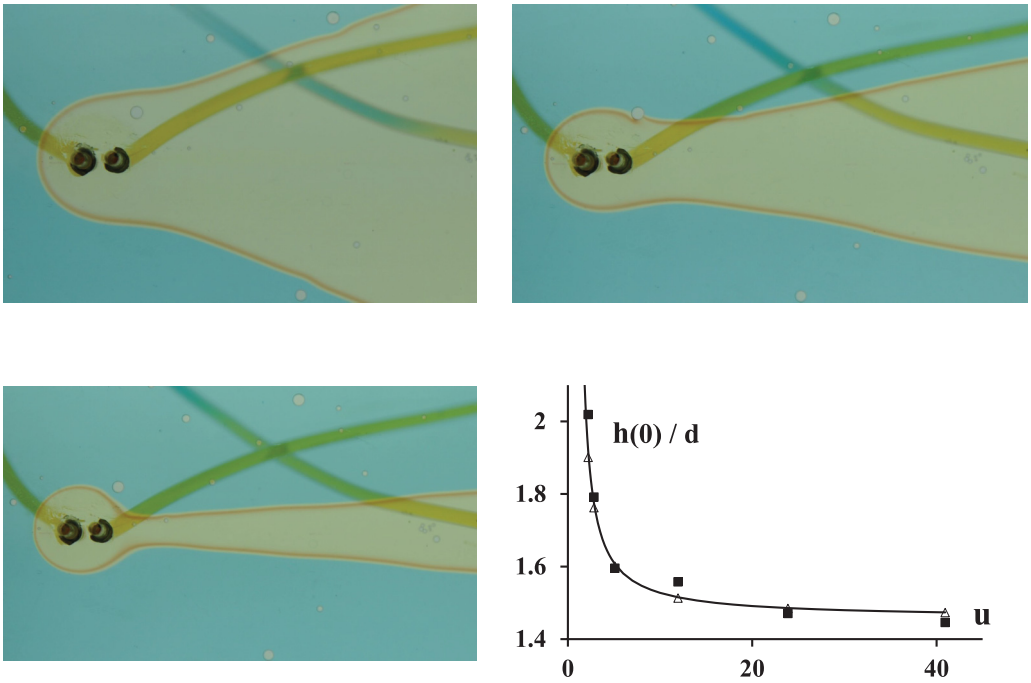

FIG. 4. Frozen chemical front in a flow around a hydrodynamic dipole. The fresh, blue reactant is injected from left to right as in Fig. 1 at a flow at constant velocity U_0. The "solid" obstacle is mimicked by a hydrodynamic dipole. Burnt, yellow fluid flows out of the leftmost hole (source) and into the other one (sink) at the same flow rate ($U_+ = -U_-$); the distance between holes is $d = 5$ mm and $l_\chi/d = 0.04$. In all the pictures, the ratio between U_0 and U_+ remains the same, and the radius of the immaterial obstacle remains, therefore, constant (see the text); $R = 7.2$ mm. From top left to bottom left: $U_0/V_\chi = -2.6, -5.25, -12.6$. The graph on the right is a plot of the normalized distance, $|h_0|/d$, of the apex of the front to the dipole on the symmetry axis vs $u = |U_0/V_\chi|$. The continuous line through the data is the prediction obtained from the eikonal with the experimental value of $l_\chi/d = 0.04$. The open triangles correspond to the selection with $l_\chi/d = 0$ (order zero). The tracks superimposed on the fluids are shadows of tubing.

cell width and thickness. The "solid" obstacle is mimicked by a hydrodynamic dipole (yellow). Burnt yellow flows out of the leftmost hole (source) and into the other one (sink) at the same flow rate ($Q_+ = -Q_-$); the distance between holes is $d = 5$ mm. The strength of the hydrodynamic dipole [26,27] is $p = d(Q_+/e)$, so that the solid disk radius involved in this velocity field is from Eq. (16):

$$R^2 = \frac{p}{2\pi U_0} = \frac{Q_+}{Q_0}\frac{wd}{2\pi}. \tag{17}$$

Therefore, keeping constant the ratio Q_+/Q_0 provides an immaterial solid disk of constant radius in a uniform flow field U_0.[1]

The three pictures in Fig. 4 display the frozen fronts achieved at different flow rates while keeping $Q_0/Q_+ = 1$ so that $R = 7.2$ mm. The figure at the bottom right is a plot of the position $|h_0|/d$ of the front on the symmetry axis versus the reduced flow rate $u = |U_0/V_\chi|$: the squares are the experimental data, and the continuous line is the theoretical prediction obtained using the above

[1]Here we have a real source and sink, the far field of which is that of a dipole. Therefore, instead of the dipole flow, we use, for the selection calculations, the velocity field of a source and a sink distant of d [26] that is closer to the experimental velocity field, especially for the near field. As a result, in the case of Fig. 4, instead of a virtual solid disk of radius $R = 7.2$ mm, the solid is closer to an ellipse of semiaxis 7.6 and 5 mm.

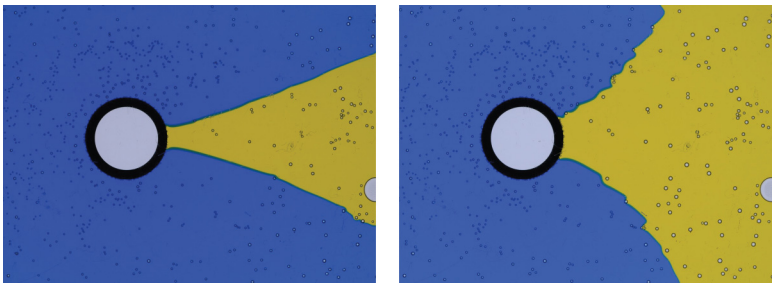

FIG. 5. The second class of experimental frozen front in a flow around a circular disk in a Hele-Shaw cell corresponds to an initial condition in which the front is in contact with the disk. The left picture is obtained for a normalized flow velocity ($U_0/V_\chi = -2.5$), which is the same as the one of the left picture of Fig. 1; therefore, for the same flow velocity, two types of frozen fronts are observable: an upstream front that avoids the solid, and a downstream one originating from the solid disk. Right: the downstream FF for $U_0/V_\chi = -1.4$.

procedure assuming an eikonal equation with the experimental, rather small, value of $l_\chi/d = 0.04$: the agreement is quite reasonable, validating both the relevance of the eikonal equation in such an experiment and the selection procedure. It is worth noting that, for such a small l_χ/d value, the theoretical prediction for $l_\chi = 0$ (open triangles in Fig. 4) is very close to the continuous line.

VI. TWO TYPES OF FROZEN FRONT IN UNIFORM FLOW PAST A SOLID DISK

As already described (Fig. 1) for $u > 1$, "upstream" frozen fronts are observed. These fronts avoid touching the disk surface and correspond to an initial front generated on the left of the disk, far upstream. For the same velocity u, but with an initial front in contact with the disk, we observed (Fig. 5) another class of frozen fronts: the fronts remain in contact at subsequent times, leading to a "downstream" FF with two symmetric branches. In Fig. 5, we see that, when u is increased, the two branches of the front become closer to the symmetry axis.

For $u \gtrsim 5 - 6$, the separation between the two branches becomes thinner and thinner as u increases, which can lead to a pinch-off followed by a detachment as observed in Ref. [17], hence no frozen fronts are observed. These new downstream frozen fronts that remain in contact with the disk surface deserve a deeper analysis. Indeed, in the experiments it is rather difficult to vary the two control parameters l_χ and V_χ over a wide range. We will address this issue with numerical simulations.

VII. PHASE DIAGRAM OF A DIFFERENT CLASS OF FROZEN FRONTS AROUND A SOLID DISK

In the experiments (Figs. 1 and 5) we have been able to observe an upstream FF avoiding the obstacle and a downstream one in contact with the solid disk. We want to draw the phase diagram of these two types of frozen front. To cover a wide range of (u,l_χ/R) values, numerical simulations of the full convection reaction diffusion equation (CRD) Eq. (2) are more suitable than experiments, especially for the control parameter l_χ/R. For that purpose, we performed two-relaxation-time (TRT) lattice Boltzmann simulations [29]. We use a 2D 400 × 1000 lattice (Fig. 6) with a solid of size 80 lattice unit diameter. In the low Reynolds number limit, we first compute the velocity field around this solid disk with periodic boundary conditions at the top and bottom and a constant flux from left to right (U_0). We wait until a stationary flow field is achieved. Then we trigger the reaction with a straight vertical product line either upstream (left) of the solid disk (top left in Fig. 6) or in contact with the solid disk on the right (top third picture from the left in Fig. 6). The chosen values of the reaction characteristics (V_χ and l_χ) [18] fix the two control parameters of the simulation, namely $u = |U_0/V_\chi|$ and l_χ/R (propagation from left to right in the absence of flow).

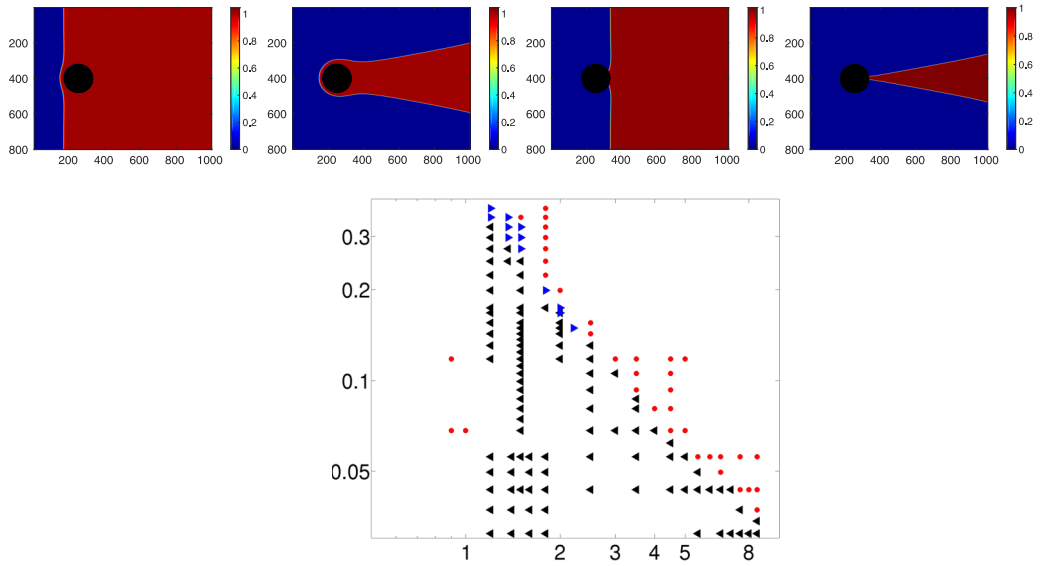

FIG. 6. Top row: from left to right, two sets of the initial condition and the corresponding frozen front. The bottom diagram is a log-log map of the observations of the two types of fronts as a function of l_χ/R (vertical scale) and $u = |U_0/V_\chi|$ (horizontal scale) in which the red dots (•) correspond to unsteady fronts, the black ◀ to observation of both upstream and downstream frozen fronts, and the blue ▷ to downstream frozen fronts only.

As both the flow and the reaction take place, the front develops, deforms, and can achieve a stationary, time-independent, shape: we observe, depending on the initial conditions, a frozen front either upstream of the disk or a downstream link on the solid surface, as seen in Fig. 6. Therefore, our numerical simulations are able to reproduce the experimental observations of the two types of observed frozen fronts. For a constant l_χ/R as the uniform flow velocity U_0 is increased, we observe the following: for $u < 1$, there is no stationary front, the front propagates continuously toward the left; for $1 < u < u_m$, the two types of frozen fronts can be achieved, whereas a further increase of u leads to both fronts detaching and propagating toward the right. This is in agreement with the experimental observations, although for a single experimental l_χ value. In the simulations, we can also increase the chemical length at a constant flow rate: above a certain $l_{\chi m}$, both types of fronts are unable to remain stationary. As discussed below, the values of u_m and $l_{\chi m}$ can be slightly different for the two types of fronts. There is a hierarchy between the stability of the upstream and downstream fronts: for all the pairs of values of $(u, l_\chi/R)$, for which an upstream front is observed, one may also observe a downstream one (black ◁) in Fig. 6. In a small window of $(u, l_\chi/R)$ values, we observe instead only the downstream frozen fronts (blue ▷). This greater stability of the downstream frozen front is demonstrated in the middle row of Fig. 7, where the upstream front barely tried to freeze upstream around the solid disk but failed, whereas it succeeded downstream. The diagram on Fig. 6 is a log-log plot of l_χ/R versus $u = |U_0/V_\chi|$ in which the red dots correspond to unsteady fronts. This diagram clearly shows that increasing either $u = |U_0/V_\chi|$ or l_χ/R while keeping the other constant leads to the disappearance of frozen fronts. This can be easily understood at least qualitatively: increasing the flow velocity moves the upstream frozen front toward the disk while the downstream one gets closer to the downstream branches. As a result, when the velocity is increased, the upstream front ends up touching the solid from the left, whereas the two downstream branches end up touching. We observe the same effect by increasing l_χ. More quantitatively, on the log-log plot of Fig. 6 the boundary between frozen fronts and unsteady fronts is an almost straight line of slope -1, that is, $u \sim R/l_\chi$. This variation may be accounted for as follows. Physically, the threshold corresponds to the rightmost extension of the front touching the disk; the front extension on the symmetry axis is

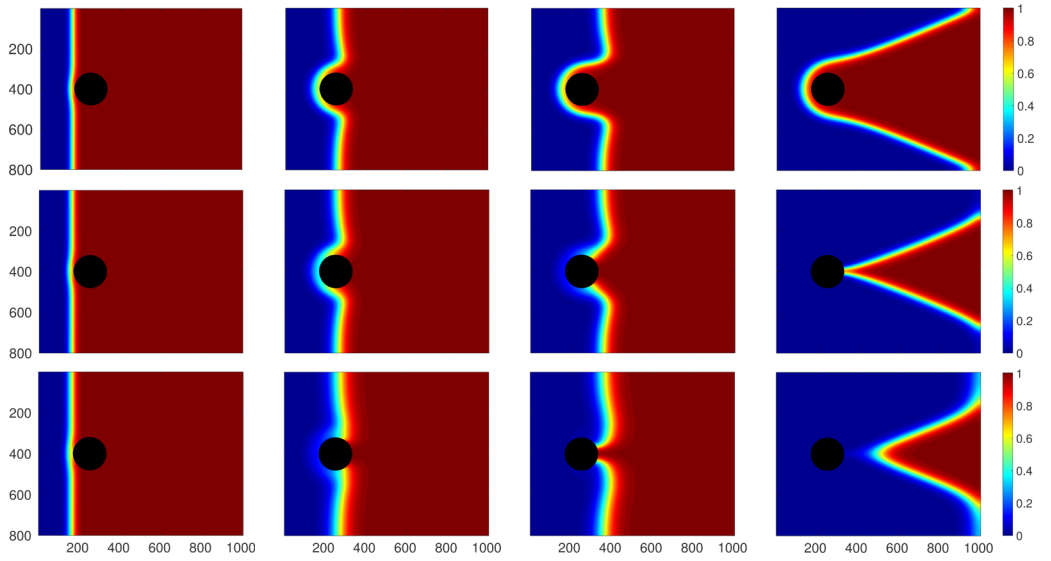

FIG. 7. Successive pictures of a front generated on the left of the disk (upstream conditions) for $u = 1.5$. Top row, $l_\chi/R = 0.25$: development of an upstream front. Middle row, $l_\chi/R = 0.27$: the front fails to freeze upstream, whereas it freezes downstream. Lower row, $l_\chi/R = 0.35$: the front is neither able to freeze upstream nor downstream and propagates toward the right.

roughly $\pm l_\chi$ around h_0; the contact with the disk, and hence the lack of a frozen front, corresponds to $|h_0| - l_\chi \sim R$. On the solid surface, $v_x(h_0 + l_\chi, 0) = 0$. In this vicinity, $v_x(x,0) \approx U_0 f(x/R)$ (Stokes flow [26]), then at first order, $v_x(h_0,0) = -\partial_x v_x(0,0) l_\chi = -(U_0/R) f'(0) l_\chi \approx U_0 l_\chi/R$. From Eq. (7), the flow velocity on the axis is balanced by the chemical velocity, $v_x(h_0,0) = V_\chi$, leading to $U_0/U_\chi \approx R/l_\chi$, in agreement with the slope on the diagram.

VIII. SIMULATION AT FINITE l_χ VERSUS THE EIKONAL LIMIT

In the previous section, we reported accurate numerical simulations of the frozen fronts, $C(x,y)$, for different chemical lengths l_χ (and flow rates). Therefore, this is a good opportunity to compare these simulations with the eikonal limit obtained in the corresponding section. On the left of Fig. 8, we have plotted the normalized apex $|h(0)|/R$ from the numerical simulations versus l_χ/R for $u = 2$. The value of $h(0)$ corresponds, respectively, to the isoconcentration lines $C = 0.25$, 0.5, and 0.75. In the same figure, the black squares correspond to the numerical integration of the eikonal equation, and the continuous line corresponds to the truncation procedure (second order) on the same velocity field as the numerical one. If the trend is the same, especially at low l_χ values, neither of the isoconcentration lines matches with the eikonal one. This is more evident in the right of the same figure, where the isoconcentration map from the simulation and the profile of the eikonal frozen front are superimposed for $v = 1.5$ and $l_\chi/R = 0.037$. Even for such a small l_χ, a discrepancy still remains. Of course we cannot expect that the single concentration jump eikonal curve matches with the $C = 0.5$ isoconcentration of the simulation, but the difference is surprising, especially far away from the solid disk where the velocity field is uniform, $\overrightarrow{U} = \overrightarrow{U_0}$. Let us try to understand this difference. The eikonal line is a straight line with an angle θ_0 with the x axis along $\overrightarrow{U_0}$. The eikonal equation (4), $\overrightarrow{U_0}\overrightarrow{n} + V_\chi = 0$, reads $U_0 \sin\theta_0 = V_\chi$. In Fig. 8, we measure $\theta_0 = (40 \pm 2)^\circ$ in agreement with the eikonal expectation $1/\sin\theta_0 = 1.55 \pm 0.05$, in reasonable agreement with $v = 1.5$.

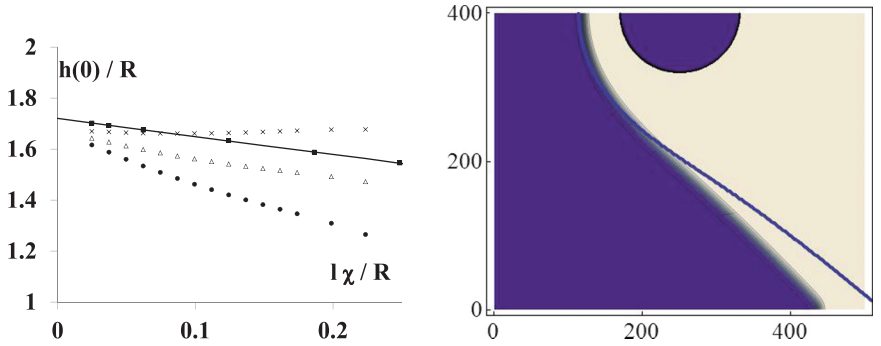

FIG. 8. Left: normalized apex distance to the disk $|h(0)|/R$ vs l_χ/R for $u = 1.5$. The circles, triangles, and $\times$ correspond to the numerical simulations where the apex is determined from the three isoconcentrations $C = 0.25$, 0.5, and 0.75. The squares correspond to the numerical integration of the eikonal equation, and the continuous line corresponds to the second order above the truncation procedure. Right: superposition on the same graph of the isoconcentration map from the simulation and of the eikonal front (solid curve) for $u = 1.5$ and $l_\chi/R = 0.037$.

A closer analysis of the simulations shows that the isoconcentration curves are nearly perfectly straight lines parallel to one another with an angle $\theta > \theta_0$ with the x axis. In the direction z perpendicular to these isoconcentrations, the concentration is well fitted by an expression similar to that applying to the chemical front in the absence of flow [Eq. (3)]: $C(z) = [1 + \exp -(\frac{z}{w})]^{-1}$, but with a width $w = 3.5$ larger than $l_\chi = 3$. As the isoconcentration curves are parallel straight lines, we can integrate the steady convection diffusion reaction Eq. (2) along z from $-\infty$ to ∞, which is merely the balance between convective flux and reaction, leading to

$$U_z = U_0 \sin\theta = V_\chi \frac{w}{l_\chi}, \tag{18}$$

where $U_z = U_0 \sin\theta$ is the projection of the uniform velocity on the normal to the isoconcentrations.

When w is larger than l_χ, $\theta > \theta_0$, in agreement with what is observed in Fig. 8: $\theta = \simeq 45^\circ$, leading to $\sin\theta \simeq 0.7$, in agreement with Eq. (18). These observations deserve further comments. Even if the chemical length is very small compared to the disk size ($l_\chi/R \simeq 0.037$), we are not in the full eikonal regime $l_\chi \to 0$, as already observed [9]. The extension of the front, $\sim l_\chi$, still matters; in this uniform flow region, the isoconcentrations can adapt their spreading (w) as well as their orientation to fulfill the CRD, whereas the eikonal front has only the orientation freedom.

IX. FREE BOUNDARY CONDITIONS AT THE DISK SURFACE: EXPERIMENTS WITH AN AIR BUBBLE

The experiments with the dipole design have proven the relevance of the eikonal limit to account for the shape of frozen fronts around an immaterial obstacle. The problem would not be so easy for a front originating from the solid surface. In the eikonal limit, the front cannot be static: at the solid surface, the flow velocity vanishes, $\vec{U} = \vec{0}$, and unless the curvature at the surface is of the order of l_χ, the only possibility left from Eq. (4) is $\vec{V_F} = \vec{V_\chi}$, as already discovered [6].

To get rid of this lack of velocity at the disk surface, we perform experiments with an air disk, namely an air bubble squeezed between the two plates of the Hele-Shaw cell: the boundary conditions between these two fluids (air and chemical solution) are the previous one of zero normal velocity [$v_r(R) = 0$], but the free boundary allows for a nonzero tangential velocity v_θ at the bubble surface [Eq. (16)]. Moreover, at this surface there is no flux of matter ($\vec{\nabla} C \cdot \vec{n} = 0$) leading to a front perpendicular to the surface. Therefore, the eikonal equation at the surface reduces to $v_\theta(R) = V_\chi$. Figure 9 displays pictures of the front on a bubble for different flow rates. Compared to the solid

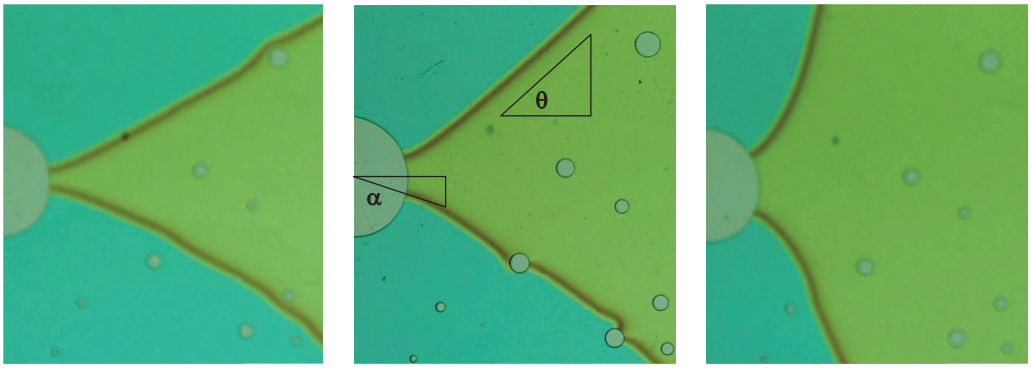

FIG. 9. Frozen chemical front in a flow around an air bubble of diameter 10 mm in a Hele-Shaw cell at different flow rates. Compared to Fig. 1, where the disk is solid, the front is perpendicular to the bubble surface. From left to right: $u = 2.1$, 1.5, and 1.05. The angle θ in the middle picture is the far-field one, whereas α is the angle expected at the bubble surface calculated from the eikonal relationship (see the text).

disk (Fig. 1), the front is perpendicular to the bubble surface at their contact point, as expected from the eikonal equation. To be more quantitative as to the relevance of this eikonal equation, we have measured the slopes (or the angle with the symmetry axis) of the straight part of the front at the bubble surface (angle α) and far away from the bubble (θ) where the flow is uniform (U_0).

Applying the eikonal equation in the far field, we obtain $U_0 \sin(\theta) = V_\chi$, whereas at the bubble surface where the tangential velocity is known from the potential flow [Eq. (16)], we get $2U_0 \sin(\alpha) = V_\chi$. Therefore, we can expect the relationship $2\sin(\alpha) \simeq \sin(\theta)$ between α and θ. Our measurements of α and θ are in reasonable agreement with this eikonal expectation: In the middle picture of Fig. 9, we provide θ and the corresponding expected $\alpha = \arcsin(\sin(\theta)/2)$, in reasonable agreement with the front position on the bubble surface.

X. CONCLUSION

We have reported experiments, analytical computations, and numerical simulations with the autocatalytic iodate-arsenious acid reaction (IAA) over a wide range of flow velocities around a solid disk. For the same set of control parameters, we observe two types of frozen fronts: an upstream FF, which avoids the solid disk, and a downstream FF with two symmetric branches emerging from the solid disk surface. We have mapped the range over which we observe these frozen fronts. We also revisited the so-called eikonal, thin front limit in order to describe the observed fronts and to select the frozen front shapes.

ACKNOWLEDGMENT

It is a pleasure to acknowledge stimulating discussions with Jean-Pierre Hulin and Agence Nationale de la Recherche for financial support of the project LaboCothep ANR-12-MONU-0011.

[1] S. K. Scott, *Oscillations, Waves, and Chaos in Chemical Kinetics*, edited by Oxford Chemistry Primers (Oxford University Press, Oxford, 1994).

[2] R. A. Fisher, The wave of advance of advantageous genes, Ann. Eugen. **7**, 355 (1937).

[3] A. N. Kolmogorov, I. Petrovsky, and N. Piscounoff, Study of the diffusion equation with growth of the quantity of matter and its application to a biology problem, Bull. Univ. Moscow, Ser. Int. A **1** (1937).

[4] Y. B. Zeldovich and D. A. Frank-Kamenetskii, A theory of thermal propagation of flame, Zh. Fiz. Khim. **12**, 100 (1938).
[5] B. Audoly, H. Berestycki, and Y. Pomeau, Réaction-diffusion en écoulement stationnaire rapide, C. R. Acad. Sci. Paris, Ser. II B **328**, 255 (2000).
[6] B. F. Edwards, Poiseuille Advection of Chemical Reaction Fronts, Phys. Rev. Lett. **89**, 104501 (2002).
[7] B. F. Edwards, Propagation velocities of chemical reaction fronts advected by Poiseuille flow, Chaos **16**, 043106 (2006).
[8] M. Leconte, J. Martin, N. Rakotomalala, and D. Salin, Pattern of Reaction Diffusion Fronts in Laminar Flows, Phys. Rev. Lett. **90**, 128302 (2003).
[9] M. Leconte, J. Martin, N. Rakotomalala, and D. Salin, Mixing and reaction fronts in laminar flows, J. Chem. Phys. **120**, 7314 (2004).
[10] D. A. Vasquez, Convective chemical fronts in a Poiseuille flow, Phys. Rev. E **76**, 056308 (2007).
[11] M. Leconte, N. Jarrige, J. Martin, N. Rakotomalala, D. Salin, and L. Talon, Taylor's regime of an autocatalytic reaction front in a pulsative periodic flow, Phys. Fluids **20**, 057102 (2008).
[12] M. E. Schwartz and T. H. Solomon, Chemical Reaction Fronts in Ordered and Disordered Cellular Flows with Opposing Winds, Phys. Rev. Lett. **100**, 028302 (2008).
[13] K. A. Mitchell and J. R. Mahoney, Invariant manifolds and the geometry of front propagation in fluid flows, Chaos **22**, 037104 (2012).
[14] D. Bargteil and T. Solomon, Barriers to front propagation in ordered and disordered vortex flows, Chaos **22**, 037103 (2012).
[15] P. W. Megson, M. L. Najarian, K. E. Lilienthal, and T. H. Solomon, Pinning of reaction fronts by burning invariant manifolds in extended flows, Phys. Fluids **27**, 023601 (2015).
[16] J. R. Mahoney, J. Li, C. Boyer, T. Solomon, and K. A. Mitchell, Frozen reaction fronts in steady flows: A burning-invariant-manifold perspective, Phys. Rev. E **92**, 063005 (2015).
[17] S. Atis, S. Saha, H. Auradou, J. Martin, N. Rakotomalala, L. Talon, and D. Salin, Chemo-hydrodynamic coupling between forced advection in porous media and self-sustained chemical waves, Chaos **22**, 037108 (2012).
[18] S. Saha, S. Atis, D. Salin, and L. Talon, Phase diagram of sustained wave fronts opposing the flow in disordered porous media, Europhys. Lett. **101**, 38003 (2013).
[19] S. Atis, S. Saha, H. Auradou, D. Salin, and L. Talon, Autocatalytic Reaction Fronts Inside a Porous Medium of Glass Spheres, Phys. Rev. Lett. **110**, 148301 (2013).
[20] S. Atis, A. Kumar Dubey, D. Salin, L. Talon, P. Le Doussal, and K. Jörg Wiese, Experimental Evidence for Three Universality Classes for Reaction Fronts in Disordered Flows, Phys. Rev. Lett. **114**, 234502 (2015).
[21] J. Mahoney, D. Bargteil, M. Kingsbury, K. Mitchell, and T. Solomon, Invariant barriers to reactive front propagation in fluid flows, Europhys. Lett. **98**, 44005 (2012).
[22] A. Hanna, A. Saul, and K. Showalter, Detailed studies of propagating fronts in iodate oxidation of arsenous acid, J. Am. Chem. Soc. **104**, 3838 (1982).
[23] T. Yoshinaga, M. Tsuschida, Y. Toyose, H. Hiratsuka, and M. Yamaye, Polyvinyl alcohol as a useful indicator on iodometry (ii): Temperature dependence of iodine recovery and the correction method of iodine concentration in the lower detection limit region, Anal. Sci. **20**, 549 (2004).
[24] M. Böckmann and S. C. Müller, Growth Rate of the Buoyancy-Driven Instability of an Autocatalytic Reaction Front in a Narrow Cell, Phys. Rev. Lett. **85**, 2506 (2000).
[25] H. J. S. Hele-Shaw, On the motion of a viscous fluid between two parallel plates, Nature (London) **58**, 34 (1898).
[26] E. Guyon, J. P. Hulin, L. Petit, and C. D. Mitescu, *Physical Hydrodynamics*, 2nd ed. (Oxford University Press, New York, 2015).
[27] H. Lamb, *Hydrodynamics*, 6th ed., edited by H. Lamb (Cambridge University Press, Cambridge, 1932).
[28] J. S. Lee and Y. C. Fung, Stokes flow around a circular cylindrical post confined between two parallel plates, J. Fluid Mech. **37**, 657 (1969).
[29] I. Ginzburg, D. d'Humières, and A. Kuzmin, Optimal stability of advection-diffusion lattice Boltzmann models with two relaxation times for positive/negative equilibrium, J. Stat. Phys. **139**, 1090 (2010).